

Non-Abelian charge conversion in bilayer binary honeycomb lattice systems

Chiranjit Mondal,^{*} Rasoul Ghadimi,^{*} and Bohm-Jung Yang[†]

Department of Physics and Astronomy, Seoul National University, Seoul 08826, Korea
Center for Theoretical Physics (CTP), Seoul National University, Seoul 08826, Korea and
Institute of Applied Physics, Seoul National University, Seoul 08826, Korea

(Dated: November 12, 2024)

In two-dimensional systems with space-time inversion symmetry, Dirac nodes (DNs) carry non-Abelian topological charges which induce intriguing momentum space braiding phenomenon. Although the original idea was proposed in condensed matter setup, the experimental verification of non-Abelian charge conversion has been limited to artificial metamaterials because of the difficulty in identifying suitable materials in which controlled tuning of DN positions is possible. In this work, we propose bilayer binary honeycomb lattices (BBHL) as a new material platform to study the non-Abelian charge conversion phenomenon in which DN positions in momentum space can be manipulated. More explicitly, we demonstrate that layer sliding and vertical pressure serve as tunable braiding parameters controlling the non-Abelian charge conversion process which is crucial to understand the stacking-dependent electronic properties of BBHL systems. We show that the BBHL systems are a promising candidate for the experimental realization of non-Abelian phenomena of DNs in condensed matter.

Recently, the braiding properties of Dirac nodes (DNs) in two-dimensional (2D) systems, have garnered considerable attention [1–8]. In these systems, the DNs are protected by space-time inversion symmetry (I_{ST}) where I_{ST} represents either the combination of space-inversion (\mathcal{P}) and time reversal (\mathcal{T}) i.e. \mathcal{PT} for spinless systems or combination of the two-fold rotation (C_2) symmetry and \mathcal{T} i.e. $C_2\mathcal{T}$ for both the spinless and spinfull systems [9–17]. A pair of bands in I_{ST} symmetric 2D systems can have an integer topological invariant, called the Euler number. Two bands with nonzero Euler number carry several DNs in between such that the total vorticity of DNs is equal to two times of the Euler number. Thus, two DNs associated with nonzero Euler number cannot be annihilated by merging although their total Berry phase is zero modulo 2π [1]. Interestingly, the two DNs associated with nonzero Euler number can be annihilated through braiding around the adjacent band's DNs, which is neatly formulated in terms of DN vorticity reversal by crossing Dirac strings [1] or non-Abelian topological charge conversion [2–4]. It is suggested that such braiding can be realized in a three-dimensional (3D) ZrTe [3], the phononic band structure of 2D layered silicate materials [6], 2D magnetic materials with in-plane magnetization [8], optical lattices [18], photonic system [19–23], classical systems including acoustic and electric circuits [24–31] and transmission line networks [5]. Nevertheless, despite the theoretical proposals of the conversion phenomena of DN non-Abelian charges, a clean and tunable 2D electronic material platform is still required for experimental exploration in condensed matter systems. Such a platform would give a new route to explore, confirm, and understand non-Abelian braiding phenomena of DNs.

In this letter, we show that bilayer binary honeycomb lattice (BBHL) systems, such as bilayer h-BX (where X = N, P, or As), exhibit $I_{ST} = \mathcal{PT}$ symmetry that offers clean and tunable platforms to explore multi-gap topology and its non-Abelian braiding phenomena. Using tight-binding calculation and *ab-initio* simulations, we show that the braiding of DNs in these setups can easily be manipulated by external stimuli

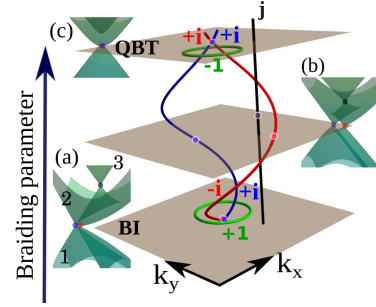


FIG. 1. Schematic representation of Dirac node (DN) braiding processes and the related charge conversion protocol in low energy three bands of honeycomb bilayer systems. (a) Two DNs with opposite charges (i , $-i$) are created by the band inversion (BI) between bands 1 and 2. Another DN exists between bands 2 and 3 with charge j . (b,c) One DN with charge $-i$ (indicated by red) encircles the DN with charge j (indicated by black) during the braiding parameter evolution and converts its charge from $-i$ to $+i$ and eventually meets with the blue DN with charge $+i$ and form a quadratic band touching (QBT) with total charge -1 . The green loop represents the charge-calculating loop enclosing the red and blue DNs. $+1$ (-1) represents the trivial (non-trivial) charge on the loops.

such as layer-sliding, pressure, and sublattice potential imbalances. The layer-sliding naturally appears in BBHL moiré systems, thus presenting them as a promising avenue for exploring multigap topology and non-Abelian charge conversion physics.

Non Abelian charge of DNs. Let us first briefly recap the idea of DN charge conversion in 2D systems with I_{ST} symmetry [1–3]. In a suitable basis where $I_{ST} = \mathcal{K}$ (\mathcal{K} is a complex conjugation operator), the Hamiltonian of the system becomes real i.e., $H(k) = H^*(k)$ [1]. For such Hamiltonian with more than two energy bands, the underlying symmetry group has a non-Abelian group structure. For instance, a three-band Hamiltonian has the generic form of $H(k) = \sum_{n=1}^3 \epsilon_n |\psi_k^n\rangle \langle \psi_k^n|$, where $|\psi_k^n\rangle$ is a real orthonormal three component vector with $O(1)$ ambiguity with the

eigenvalue ϵ_n . Therefore, the corresponding classifying space is $M_3 = O(3)/O(1)^3$ where $O(N)$ represents the orthogonal group. The homotopy group of the system is quaternion i.e., $\pi_1(M_3) = \mathbb{Q}$, a non-Abelian group which has five conjugacy classes $\{+1, -1, \pm i, \pm j, \pm k\}$ with the anti-commuting relations $ij = -ji$ and $i^2 = j^2 = k^2 = -1$ [2]. In the I_{ST} symmetric three bands labeled by 1, 2, and 3 in increasing energy order, $\pm i$ ($\pm j$) represents the charge of nodes between bands 1 and 2 (2 and 3), where \pm determine relative charges of the nodes within the same pair of bands. $+1$ indicates that no node exists or that all nodes can be annihilated pairwise, while -1 indicates a quadratic band touching or at least two DNs with the same charge [2]. In Fig. 1, we schematically show how two DNs with opposite charges ($\pm i$) are created by a band inversion [Fig. 1 (a)] and converted to a quadratic band touching (QBT) [Fig. 1 (c)]. In this process, one of the two DNs changes its sign by encircling a DN of adjacent bands with charge j [Fig. 1 (b)]. This charge conversion process is called non-Abelian braiding of DNs. Therefore, the I_{ST} symmetric band nodes are characterized by the non-Abelian quaternion charge, which serves as the key ingredient for the non-Abelian braiding protocol and related charge conversion phenomena [2, 3] [see Supplemental Material (SM) [32] for detailed discussions on non-Abelian charges].

The relative charges of two DNs within the same bands can also be determined using the patch Euler class (χ) [3]. The patch Euler class over a patch \mathcal{D} , for two real sub-bands $|u^1(k)\rangle, |u^2(k)\rangle$ that are separated by a gap from the adjacent bands in the given patch \mathcal{D} is, [3],

$$\chi(\mathcal{D}) = \frac{1}{2\pi} \left[\int_{\mathcal{D}} \text{Eu}(\mathbf{k}) dk_x dk_y - \oint_{\partial\mathcal{D}} \mathbf{a}(\mathbf{k}) \cdot d\mathbf{k} \right], \quad (1)$$

where Euler connection and Euler form are given by $\mathbf{a}(\mathbf{k}) = \langle u^1(k) | \nabla_{\mathbf{k}} u^2(k) \rangle$, and $\text{Eu}(\mathbf{k}) = \langle \nabla_{\mathbf{k}} u^1(\mathbf{k}) | \times | \nabla_{\mathbf{k}} u^2(\mathbf{k}) \rangle$, respectively [1, 3]. The patch Euler class for a single DN is $\chi = \pm \frac{1}{2}$, where its sign depends on their charges and making it $\chi = \frac{1}{2} + \frac{1}{2} = 1$ (non-trivial) or $\chi = \frac{1}{2} - \frac{1}{2} = 0$ (trivial) when two DNs with same or opposite charges reside inside the patch. In the following, we use the patch Euler class to discuss braiding phenomena in the BBHL system where layer-shifting/moiré-potential or pressure can be employed as the tunable braiding parameters.

Layer sliding as a braiding parameter-. Our model is motivated by the energy band structure of bilayer graphene (BLG) with I_{ST} symmetry. It is known that BLG has two highly symmetric stacking configurations, AB and AA stacking [33]. AB stacking provides the well-known QBT at the Brillouin zone corner K and K' whereas AA stacking gives a nodal line at K and K' [34–37]. These stacking can be smoothly transformed to each other by layer sliding in $I_{ST} = \mathcal{PT}$ symmetric manner as shown in Fig. 2(a). The inversion center is indicated by the pink circle in Fig. 2(a) which connects the same sublattice in the top and bottom layers. The green arrow represents the direction of layer sliding. If $r = 0$ ($r = 1$), the stacking becomes identical to the AB (AA) configurations. An arbitrary

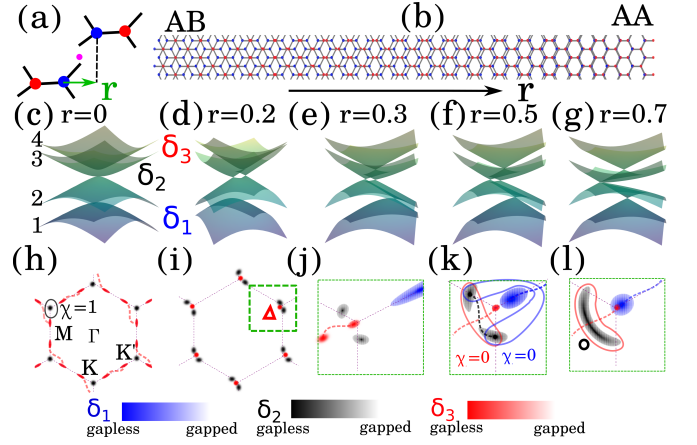


FIG. 2. Layer sliding as a braiding parameter. (a) Hexagonal bilayer with two sublattices indicated by blue and red dots. The different stacking configurations can be generated by shifting one layer with respect to the other layer (indicated by green arrow r). The pink dot in (a) represents the inversion centers that connect the two same-colored sites in the top and bottom layers, respectively. (b) A snapshot of moiré of hexagonal bilayer that connects AB ($r = 0$) to AA ($r = 1$) stacking. For large moiré length, a local position on (b) can be considered as a bilayer system with a certain amount of shifting. (c-g) Energy dispersion (around one valley) for various r and three gaps represented by δ_1 , δ_2 , and δ_3 between the band 1,2,3, and 4. (h,i) The distribution of the gap size $|\delta_{1,2,3}|$ in the Brillouin zone (j-l) $|\delta|$ distribution near K valley. The dotted lines in (h-l) are Dirac strings, which can flip the topological charge of the adjacent DN after crossing. \circ and \triangle represent the regions where creation and annihilation of DNs occurs, respectively. The blue, black, and red color bars at the bottom indicate the gapless (dark color) and gapped (light color) regions in δ_1, δ_2 , and δ_3 gap respectively, in the momentum space.

value of r corresponds to a stacking between AB and AA configurations which can be achieved by layer sliding. All such stacking configurations can also naturally appear in suitable moiré lattice [see Fig. 2(b)], where locally atomic stacking resembles two graphene layers with a certain amount of sliding r . Additionally, different stacking of BLG and its moiré structures already has been constructed in metamaterials providing further tunable setup to study our proposed braiding phenomena [38–41].

Fig. 2(c-g) shows the evolution of energy dispersion around K with the corresponding nodal structures in (Fig. 2(h-l)) upon increasing r , which shows that the topologically protected QBT at $r = 0$ splits into two DNs that migrate in momentum space until they are pair-annihilated as r increases. We use small sublattice potential which respects $I_{ST} = \mathcal{PT}$, to complete the braiding process as AA stacking without sublattice mass results in nodal loops [37]. This sublattice mass can be generated, for instance, by electronic instabilities [42, 43] or mimicking systems such as bi-layers h-BX (X = P and As) [44]. As each layer has two sublattices, we obtain four energy bands (denoted by 1,2,3, and 4 in Fig. 2(c)). Three energy gaps between the bands are δ_1 [between 1 and 2], δ_2 [between 2 and 3], and δ_3 [between 3 and 4] [see SM for the details of

the *tight-binding* and *ab-initio* calculations].

Fig. 2(h-l) shows the gap values of $|\delta_{1,2,3}|$, represented by blue, black, and red colors in the three gaps. The dark blue, black, and red color indicates the gapless nodal points in the δ_1 , δ_2 , and δ_3 , respectively. Fig. 2(h) shows that the energy dispersion contains DNs near the M (red nodes) point in the δ_1 gap and the QBT (black nodes) in the δ_2 gap at K/K' . We obtain that χ of the QBT for the region indicated by the black circle around K in Fig. 2(h) gives $\chi = 1$, and confirms that the QBT is topologically protected. At $r = 0.2$, the QBT splits into two DNs (black nodes) [see Fig. 2(d,i)]. Also, at the same time, some of the DNs undergo pair annihilation and pair creation in other gaps. The region where pair-annihilation (pair-creation) occurs is indicated by the “O” (“ Δ ”) symbol. At $r = 0.2$, a pair of DNs (red nodes) is generated in the δ_3 gap as shown in Fig. 2(d, i) around K and K' . Fig. 2 (j) shows the magnified view of the nodal structure around K for $r = 0.3$ which shows one red node remains near K/K' while the other moves towards the center of BZ. At $r \approx 0.5$, one DN in δ_1 gap (blue nodes) moves towards the K [see Fig. 2(f, k)]. In this situation, two black nodes in the δ_2 gap stay with the largest separation in momentum space. We compute the χ of these two black DNs in two patches shown by blue and red loops in Fig. 2(k), both of which give a trivial Euler class (i.e. $\chi = 0$). Therefore the two black nodes on the red or blue patch have opposite charges and can undergo pair-annihilation without any topological obstruction [Fig. 2(g,l)].

To intuitively understand the role of braiding protocol, we connect the DN pairs (within the same gap) using dashed lines to represent their Dirac strings [1]. As mentioned earlier, a DN flips its sign when it encircles adjacent band DNs. Dirac strings provide a useful tool to determine whether a Dirac cone has undergone such an encircling process [1]. Intuitively, a Dirac string arises as a consequence of the π Berry phase associated with the DN, where the wave function in the real basis exhibits a phase discontinuity when smoothly sweeping the loop that encloses a DN. If two DNs initially have the same charges, after one of them crosses a Dirac string between DNs in adjacent gaps, they become to carry the opposite charges as shown in Fig. 2(h-l). Accordingly, with increasing r , two black DNs with the same charges eventually become oppositely charged when they move inside the red patch crossing the red Dirac string, and thereby become pair-annihilated after the collision as shown Fig. 2(k-l).

In summary, the two black DNs, which initially carry the same charges $(+i, +i)$, turn into carrying the opposite charge $(+i, -i)$ after one of them encircles a red DN, thus eventually becomes pair-annihilated. Note that flipping the sign of sublattice potential $m \rightarrow -m$ mediates braiding with the annihilation process inside the blue patch in Fig. 2(k) (discussed in SM). In the case of BLG with $m=0$, the braiding process is not completed, even when r varies from 0 to 1, because the final AA-stacked state with $r = 1$ possesses a nodal line at the Fermi level protected by mirror symmetry ($\mathcal{M}_z : z \rightarrow -z$) [36, 37].

Pressure as a braiding parameter. Let us propose another

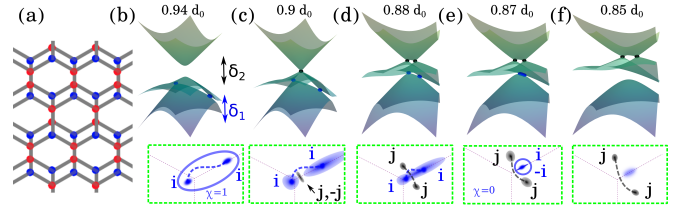


FIG. 3. Pressure-induced braiding. (a) A bilayer honeycomb lattice with a small shift ($r = 0.1$) of one layer from AB configuration. (b-f) The dispersion energy (upper panel) and configuration of the gapless region in momentum space near K point (lower panels) are plotted with decreasing interlayer distance (increasing pressure). d_0 is the interlayer distance of BLG. χ becomes non-trivial to trivial during the evolution.

braiding protocol in BBHL induced by pressure. We find that under external pressure, a braiding mechanism mediates the transportation of DNs from one gap to the other gap. To simulate the pressured BBHL, we decrease the interlayer distance in both the *tight-binding* model and DFT calculations.

In the following, we show the non-Abelian charge conversion using the *tight-binding* model. (see SM for the DFT results). Fig. 3(a) shows BBHL stacking with $r = 0.1$. We consider the three lower bands and two gaps δ_1 and δ_2 between the bands. For large sublattice potential $m = -0.4eV$ (mimicking h-BX), two DNs with the same charge (i, i) are initially located in the δ_1 gap [Fig. 3(b)]. At the interlayer distance $0.9d_0$ where d_0 indicates the interlayer distance of pristine bilayer graphene [Fig. 3(c)], a band touching happens in the δ_2 gap which creates a pair of DNs in δ_2 gap (black nodes) with opposite charges $(j, -j)$ though the BI. Further reduction of interlayer distance [Fig. 3(d)] separates black DNs and one of them crosses the blue Dirac string. Therefore the mutual charges of black nodes are converted from $(j, -j)$ to (j, j) . With additional pressure [Fig. 3(e)] the blue nodes cross the black Dirac strings and their charges are converted from (i, i) into $(-i, i)$. As such the blue nodes in δ_1 gap are annihilated after mutual collision [Fig. 3(e,f)]. The transportation of DNs from δ_1 gap to δ_2 gap occurs by the non-Abelian braiding and a sequence of charge conversion processes. In SM, we discuss the charge conversion process for various m and interlayer distance/pressure which exhibit similar phenomena. For the AB stacking (i.e. $r = 0$), the two DNs combine to form a QBT because of the underlying C_{3z} rotation symmetry, making the visualization of the Dirac string difficult. Nonetheless, the transportation of the QBT from one gap to another gap occurs by the non-Abelian braiding when the external pressure is tuned (see SM). However, the nodal transition always passes through a triple point degeneracy (TDP) which makes χ ill-defined at the TDP, necessitating the frame rotation charge calculation [3] (see SM for the detail). We also note that the QBT can be unstable under trigonal wrapping. However, it does not affect the braiding phenomena (see SM).

Our DFT calculations confirm that the maximum pressure of approximately up to 12 GPa (7.5 GPa) is required in h-BP (h-BAs) for a complete braiding process (see Fig. 4(a) and SM

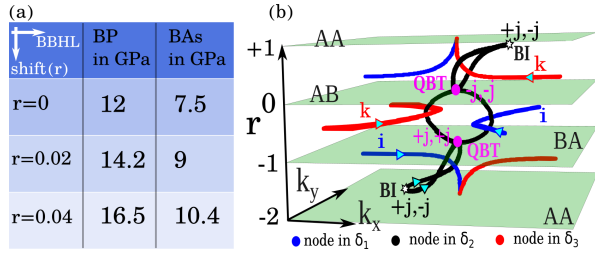


FIG. 4. (a) Maximum pressure in gigapascal (GPa) which is required to complete the braiding process in the BBHL systems BP and BAs for the specific r . (b) Summary of nodal trajectories evolution. Colored lines represent the evolution of Dirac nodes (DNs) in the gaps δ_1 [blue], δ_2 [black], and δ_3 [red], shown in Fig. 2(c), as a function of layer shifting (r) in momentum space near the K/K' points. The green planes indicate the AA, AB, and BA stacking configurations. Two black DN trajectories with opposite charges are created by band inversion (BI) near the AA stacking (at $r = -2$ and $r = +1$) and undergo braiding with adjacent bands nodes (blue or red), eventually transforming into a quadratic band touching (QBT). The QBT from the BA stacking ($r = -1$) is braided by both the blue and red nodes, but its charges remain unchanged, resulting in QBT again at the AB stacking ($r = 0$). The magenta arrows represent the direction of movement of DN trajectories when r is changed from -2 to +1.

for further detail). To apply such pressure, we decrease the interlayer distance of h-BP (h-BAs) to $0.81d_0$ ($0.85d_0$) where $d_0 = 3.69\text{\AA}$ (3.75\AA) is the relaxed interlayer distance for h-BP (h-BAs). It is important to mention that such pressure has been experimentally applied in graphite-like h-BN system where a similar amount of interlayer compression is observed [45]. Also, recent experiment demonstrated the measurement of the dynamical band structure in moiré system under external pressure [46]. In Fig. 4(a), we show the maximum pressure value (calculated using DFT) required for a specific r to complete the braiding process in the two representative BBHL systems BP and BAs.

Nodal trajectories during the braiding-. As we discussed earlier, DN trajectories in I_{ST} systems are topologically protected and can only be annihilated in pairs. By tracking the positions of these DN trajectories in momentum space, one can obtain continuous trajectories as functions of the braiding parameters. These trajectories often are intertwined with trajectories of other DN trajectories from other bands and provide complete information on the braiding processes. In Fig. 4(b), we show the nodal trajectory in momentum space (horizontal plane) around the K/K' point where layer shifting (r) acts as the braiding parameter (vertical axis). The layer stacking changes sequentially from AA ($r = -2$) to AB ($r = -1$), then to BA ($r = 0$), and finally returns to AA ($r = +1$). Near the AA stacking ($r = -2$), a BI creates two black nodes with opposite charges [we assume small m ; see SM for different m and pressure]. They go through a braiding process crossing the Dirac strings between the blue nodes, which makes them have the same charge, leading to QBT in BA stacking ($r = -1$). Then the QBT at $r = -1$ again splits into two DN trajectories which undergo two braiding processes with DN trajectories in both lower and upper gaps. This pro-

cess makes the two black DN trajectories to have the same charge, which eventually gives another QBT in AB stacking ($r = 0$). Further increasing r , the QBT of AB stacking splits into two DN trajectories which initially have the same charge but be converted to have the opposite charges after braiding around the red DN, thus eventually be pair-annihilated near AA stacking. We note that when $m=0$, the black trajectory at AA stacking evolves into a circle, which is a consequence of the nodal line in AA stacking.

Discussion-. Experimentally, the evolution of energy dispersion can be observed using current techniques such as angle-resolved photoemission spectroscopy (ARPES) [47, 48] or locally using nano-ARPES [49, 50]. Additionally, recently several proposals have been given to directly measure the charge of nodes [51] using interferometry [52] or optical responses [18]. The sliding of graphene nanoflakes on another layer of graphene has been studied using experimental techniques such as the frictional force microscope, and scanning tunneling microscopy (STM) [53]. Our proposed theory can also be studied in a meta-materials platform such as acoustic twisted bilayer graphene or photonic systems where BBHL type electronic structures were explored [40, 54–57].

C.M., R.G. and B.J.Y. were supported by Samsung Science and Technology Foundation under Project No. SSTF-BA2002-06, National Research Foundation of Korea (NRF) grants funded by the government of Korea (MSIT) (Grants No. NRF-2021R1A5A1032996), and GRDC(Global Research Development Center) Cooperative Hub Program through the National Research Foundation of Korea(NRF) funded by the Ministry of Science and ICT(MSIT) (RS-2023 00258359)).

* These authors contributed equally

† bjyang@snu.ac.kr

- [1] J. Ahn, S. Park, and B.-J. Yang, Failure of nielsen-ninomiya theorem and fragile topology in two-dimensional systems with space-time inversion symmetry: Application to twisted bilayer graphene at magic angle, *Phys. Rev. X* **9**, 021013 (2019).
- [2] Q. Wu, A. A. Soluyanov, and T. Bzdušek, Non-abelian band topology in noninteracting metals, *Science* **365**, 1273 (2019), <https://www.science.org/doi/pdf/10.1126/science.aau8740>.
- [3] A. Bouhon, Q. Wu, R.-J. Slager, H. Weng, O. V. Yazyev, and T. Bzdušek, Non-abelian reciprocal braiding of weyl points and its manifestation in zrte, *Nature Physics* **16**, 1137 (2020).
- [4] Y. Yang, B. Yang, G. Ma, J. Li, S. Zhang, and C. T. Chan, Non-abelian physics in light and sound, *Science* **383**, eadf9621 (2024), <https://www.science.org/doi/pdf/10.1126/science.adf9621>.
- [5] Q. Guo, T. Jiang, R.-Y. Zhang, L. Zhang, Z.-Q. Zhang, B. Yang, S. Zhang, and C. T. Chan, Experimental observation of non-abelian topological charges and edge states, *Nature* **594**, 195 (2021).
- [6] B. Peng, A. Bouhon, B. Monserrat, and R.-J. Slager, Phonons as a platform for non-abelian braiding and its manifestation in layered silicates, *Nature Communications* **13**, 423 (2022).
- [7] F. N. Ünal, A. Bouhon, and R.-J. Slager, Topological euler class

- as a dynamical observable in optical lattices, Phys. Rev. Lett. **125**, 053601 (2020).
- [8] S. H. Lee, Y. Qian, and B.-J. Yang, Euler band topology in spin-orbit coupled magnetic systems (2024), arXiv:2404.16383 [cond-mat.mes-hall].
- [9] T. Morimoto and A. Furusaki, Weyl and dirac semimetals with F_2 topological charge, Phys. Rev. B **89**, 235127 (2014).
- [10] C. Fang, Y. Chen, H.-Y. Kee, and L. Fu, Topological nodal line semimetals with and without spin-orbital coupling, Phys. Rev. B **92**, 081201 (2015).
- [11] C. Fang and L. Fu, New classes of three-dimensional topological crystalline insulators: Nonsymmorphic and magnetic, Phys. Rev. B **91**, 161105 (2015).
- [12] Y. X. Zhao and Y. Lu, pt -symmetric real dirac fermions and semimetals, Phys. Rev. Lett. **118**, 056401 (2017).
- [13] J. Ahn and B.-J. Yang, Unconventional topological phase transition in two-dimensional systems with space-time inversion symmetry, Phys. Rev. Lett. **118**, 156401 (2017).
- [14] J. Kim, S. S. Baik, S. W. Jung, Y. Sohn, S. H. Ryu, H. J. Choi, B.-J. Yang, and K. S. Kim, Two-dimensional dirac fermions protected by space-time inversion symmetry in black phosphorus, Phys. Rev. Lett. **119**, 226801 (2017).
- [15] J. Ahn, D. Kim, Y. Kim, and B.-J. Yang, Band topology and linking structure of nodal line semimetals with Z_2 monopole charges, Phys. Rev. Lett. **121**, 106403 (2018).
- [16] J. Ahn and B.-J. Yang, Symmetry representation approach to topological invariants in $C_{2v}t$ -symmetric systems, Phys. Rev. B **99**, 235125 (2019).
- [17] J. Ahn, S. Park, D. Kim, Y. Kim, and B.-J. Yang, Stiefel–whitney classes and topological phases in band theory, Chinese Physics B **28**, 117101 (2019).
- [18] W. J. Jankowski, A. S. Morris, A. Bouhon, F. N. Ünal, and R.-J. Slager, Optical manifestations of topological euler class in electronic materials (2023), arXiv:2311.07545 [cond-mat.mes-hall].
- [19] D. Wang, B. Yang, M. Wang, R.-Y. Zhang, X. Li, Z. Q. Zhang, S. Zhang, and C. T. Chan, Observation of non-abelian charged nodes linking nonadjacent gaps, Phys. Rev. Lett. **129**, 263604 (2022).
- [20] D. Cheng, K. Wang, and S. Fan, Artificial non-abelian lattice gauge fields for photons in the synthetic frequency dimension, Phys. Rev. Lett. **130**, 083601 (2023).
- [21] Y.-K. Sun, X.-L. Zhang, F. Yu, Z.-N. Tian, Q.-D. Chen, and H.-B. Sun, Non-abelian thouless pumping in photonic waveguides, Nature Physics **18**, 1080 (2022).
- [22] J. Noh, T. Schuster, T. Iadecola, S. Huang, M. Wang, K. P. Chen, C. Chamon, and M. C. Rechtsman, Braiding photonic topological zero modes, Nature Physics **16**, 989 (2020).
- [23] E. Yang, B. Yang, O. You, H.-C. Chan, P. Mao, Q. Guo, S. Ma, L. Xia, D. Fan, Y. Xiang, and S. Zhang, Observation of non-abelian nodal links in photonics, Phys. Rev. Lett. **125**, 033901 (2020).
- [24] Z.-G. Chen, R.-Y. Zhang, C. T. Chan, and G. Ma, Classical non-abelian braiding of acoustic modes, Nature Physics **18**, 179 (2022).
- [25] H. Qiu, Q. Zhang, T. Liu, X. Fan, F. Zhang, and C. Qiu, Minimal non-abelian nodal braiding in ideal metamaterials, Nature Communications **14**, 1261 (2023).
- [26] Y. Barlas and E. Prodan, Topological braiding of non-abelian midgap defects in classical metamaterials, Phys. Rev. Lett. **124**, 146801 (2020).
- [27] T. Jiang, Q. Guo, R.-Y. Zhang, Z.-Q. Zhang, B. Yang, and C. T. Chan, Four-band non-abelian topological insulator and its experimental realization, Nature Communications **12**, 6471 (2021).
- [28] H. Park, S. Wong, A. Bouhon, R.-J. Slager, and S. S. Oh, Topological phase transitions of non-abelian charged nodal lines in spring-mass systems, Phys. Rev. B **105**, 214108 (2022).
- [29] M. Wang, S. Liu, Q. Ma, R.-Y. Zhang, D. Wang, Q. Guo, B. Yang, M. Ke, Z. Liu, and C. T. Chan, Experimental observation of non-abelian earring nodal links in phononic crystals, Phys. Rev. Lett. **128**, 246601 (2022).
- [30] J. Wu, Z. Wang, Y. Biao, F. Fei, S. Zhang, Z. Yin, Y. Hu, Z. Song, T. Wu, F. Song, and R. Yu, Non-abelian gauge fields in circuit systems, Nature Electronics **5**, 635 (2022).
- [31] M. Ezawa, Topological euler insulators and their electric circuit realization, Phys. Rev. B **103**, 205303 (2021).
- [32] See Supplemental Material in *** which includes Refs. [1–3, 58–67].
- [33] N. T. T. Tran, S.-Y. Lin, O. E. Glukhova, and M.-F. Lin, Configuration-induced rich electronic properties of bilayer graphene, The Journal of Physical Chemistry C **119**, 10623 (2015), <https://doi.org/10.1021/jp511692e>.
- [34] A. H. Castro Neto, F. Guinea, N. M. R. Peres, K. S. Novoselov, and A. K. Geim, The electronic properties of graphene, Rev. Mod. Phys. **81**, 109 (2009).
- [35] Y. Zhang, T.-T. Tang, C. Girit, Z. Hao, M. C. Martin, A. Zettl, M. F. Crommie, Y. R. Shen, and F. Wang, Direct observation of a widely tunable bandgap in bilayer graphene, Nature **459**, 820 (2009).
- [36] C. J. Tabert and E. J. Nicol, Dynamical conductivity of aa-stacked bilayer graphene, Phys. Rev. B **86**, 075439 (2012).
- [37] C. Mondal, S. Kim, and B.-J. Yang, Unremovable linked nodal structures protected by crystalline symmetries in stacked bilayer graphene with kekulé texture, Phys. Rev. B **106**, L121118 (2022).
- [38] J. Lu, C. Qiu, W. Deng, X. Huang, F. Li, F. Zhang, S. Chen, and Z. Liu, Valley topological phases in bilayer sonic crystals, Phys. Rev. Lett. **120**, 116802 (2018).
- [39] M. Rosendo López, F. Peñaranda, J. Christensen, and P. San-Jose, Flat bands in magic-angle vibrating plates, Phys. Rev. Lett. **125**, 214301 (2020).
- [40] Y. Deng, M. Oudich, N. J. Gerard, J. Ji, M. Lu, and Y. Jing, Magic-angle bilayer phononic graphene, Phys. Rev. B **102**, 180304 (2020).
- [41] W. Dorrell, H. Pirie, S. M. Gardezi, N. C. Drucker, and J. E. Hoffman, van der waals metamaterials, Phys. Rev. B **101**, 121103 (2020).
- [42] A. L. Rakhmanov, A. V. Rozhkov, A. O. Sboychakov, and F. Nori, Instabilities of the aa-stacked graphene bilayer, Phys. Rev. Lett. **109**, 206801 (2012).
- [43] A. O. Sboychakov, A. L. Rakhmanov, A. V. Rozhkov, and F. Nori, Metal-insulator transition and phase separation in doped aa-stacked graphene bilayer, Phys. Rev. B **87**, 121401 (2013).
- [44] R. Ghadimi, C. Mondal, S. Kim, and B.-J. Yang, Quantum valley hall effect without berry curvature (2024), arXiv:2403.15050 [cond-mat.mes-hall].
- [45] V. Solozhenko, G. Will, and F. Elf, Isothermal compression of hexagonal graphite-like boron nitride up to 12 gpa, Solid State Communications **96**, 1 (1995).
- [46] M. Yankowitz, J. Jung, E. Laksono, N. Leconte, B. L. Chittari, K. Watanabe, T. Taniguchi, S. Adam, D. Graf, and C. R. Dean, Dynamic band-structure tuning of graphene moiré superlattices with pressure, Nature **557**, 404 (2018).
- [47] M. Sprinkle, D. Siegel, Y. Hu, J. Hicks, A. Tejeda, A. Taleb-Ibrahimi, P. Le Fèvre, F. Bertran, S. Vizzini, H. Enriquez, S. Chiang, P. Soukiassian, C. Berger, W. A. de Heer, A. Lan-

- zara, and E. H. Conrad, First direct observation of a nearly ideal graphene band structure, *Phys. Rev. Lett.* **103**, 226803 (2009).
- [48] C.-M. Cheng, L. F. Xie, A. Pachoud, H. O. Moser, W. Chen, A. T. S. Wee, A. H. Castro Neto, K.-D. Tsuei, and B. Özyilmaz, Anomalous spectral features of a neutral bilayer graphene, *Scientific Reports* **5**, 10025 (2015).
- [49] J. Avila, I. Razado, S. Lorcy, R. Fleurier, E. Pichonat, D. Vignaud, X. Wallart, and M. C. Asensio, Exploring electronic structure of one-atom thick polycrystalline graphene films: A nano angle resolved photoemission study, *Scientific Reports* **3**, 2439 (2013).
- [50] L. I. Johansson, R. Armiento, J. Avila, C. Xia, S. Lorcy, I. A. Abrikosov, M. C. Asensio, and C. Virojanadara, Multiple π -bands and bernal stacking of multilayer graphene on c-face sic, revealed by nano-angle resolved photoemission, *Scientific Reports* **4**, 4157 (2014).
- [51] C. D. Brown, S.-W. Chang, M. N. Schwarz, T.-H. Leung, V. Kozii, A. Avdoshkin, J. E. Moore, and D. Stamper-Kurn, Direct geometric probe of singularities in band structure, *Science* **377**, 1319 (2022), <https://www.science.org/doi/pdf/10.1126/science.abm6442>.
- [52] O. Breach, R.-J. Slager, and F. N. Ünal, Interferometry of non-abelian band singularities and euler class topology (2024), [arXiv:2401.01928 \[cond-mat.quant-gas\]](https://arxiv.org/abs/2401.01928).
- [53] X. Feng, S. Kwon, J. Y. Park, and M. Salmeron, Superlubric sliding of graphene nanoflakes on graphene, *ACS Nano* **7**, 1718 (2013), pMID: 23327483, <https://doi.org/10.1021/nn305722d>.
- [54] Y.-H. Lu, Y. Wang, Y.-J. Chang, Z.-M. Li, W.-H. Cui, J. Gao, W.-H. Zhou, H. Zheng, and X.-M. Jin, Observing movement of dirac cones from single-photon dynamics, *Phys. Rev. B* **103**, 064304 (2021).
- [55] S. M. Gardezi, H. Pirie, S. Carr, W. Dorrell, and J. E. Hoffman, Simulating twistronics in acoustic metamaterials, *2D Materials* **8**, 031002 (2021).
- [56] M. Oudich, G. Su, Y. Deng, W. Benalcazar, R. Huang, N. J. R. K. Gerard, M. Lu, P. Zhan, and Y. Jing, Photonic analog of bilayer graphene, *Phys. Rev. B* **103**, 214311 (2021).
- [57] S.-Q. Wu, Z.-K. Lin, B. Jiang, X. Zhou, Z. H. Hang, B. Hou, and J.-H. Jiang, Higher-order topological states in acoustic twisted moiré superlattices, *Phys. Rev. Appl.* **17**, 034061 (2022).
- [58] N. D. Mermin, The topological theory of defects in ordered media, *Rev. Mod. Phys.* **51**, 591 (1979).
- [59] P. E. Blöchl, Projector augmented-wave method, *Phys. Rev. B* **50**, 17953 (1994).
- [60] G. Kresse and J. Hafner, Ab initio molecular dynamics for liquid metals, *Phys. Rev. B* **47**, 558 (1993).
- [61] G. Kresse and D. Joubert, From ultrasoft pseudopotentials to the projector augmented-wave method, *Phys. Rev. B* **59**, 1758 (1999).
- [62] N. Marzari and D. Vanderbilt, Maximally localized generalized wannier functions for composite energy bands, *Phys. Rev. B* **56**, 12847 (1997).
- [63] I. Souza, N. Marzari, and D. Vanderbilt, Maximally localized wannier functions for entangled energy bands, *Phys. Rev. B* **65**, 035109 (2001).
- [64] N. Marzari, A. A. Mostofi, J. R. Yates, I. Souza, and D. Vanderbilt, Maximally localized wannier functions: Theory and applications, *Rev. Mod. Phys.* **84**, 1419 (2012).
- [65] A. A. Mostofi, J. R. Yates, G. Pizzi, Y.-S. Lee, I. Souza, D. Vanderbilt, and N. Marzari, An updated version of wannier90: A tool for obtaining maximally-localised wannier functions, *Computer Physics Communications* **185**, 2309 (2014).
- [66] G. Trambly de Laissardière, D. Mayou, and L. Magaud, Localization of dirac electrons in rotated graphene bilayers, *Nano Letters* **10**, 804 (2010).
- [67] P. Moon and M. Koshino, Optical absorption in twisted bilayer graphene, *Phys. Rev. B* **87**, 205404 (2013).

Supplemental Material for Non-Abelian charge conversion in bilayer binary honeycomb lattice systems

Chiranjit Mondal and Rasoul Ghadimi

*Department of Physics and Astronomy, Seoul National University, Seoul 08826, Korea and
Center for Theoretical Physics (CTP), Seoul National University, Seoul 08826, Korea*

Bohm-Jung Yang*

*Department of Physics and Astronomy, Seoul National University, Seoul 08826, Korea
Center for Theoretical Physics (CTP), Seoul National University, Seoul 08826, Korea and
Center for Correlated Electron Systems, Institute for Basic Science (IBS), Seoul 08826, Korea*

(Dated: November 12, 2024)

CONTENTS

S1. Introduction	1
S2. Braiding protocols	1
S3. DFT computational details	2
S4. Tight-binding details	3
S5. Frame charge and braiding for AB stacking	3
S6. DFT simulations for h-BX (B=Boron, X= P (Phosphorus), and As (Arsenic))	4
S7. Effect of trigonal wrapping	5
S8. Edge mode evolution during braiding parameters tuning	6
S9. Nodal trajectories for different sublattice potentials and layer distance	7
References	7

S1. INTRODUCTION

In this Supplemental Material, we first give an introduction to general idea of non-Abelian braiding in S2. We also discuss the detail of the DFT and tight-binding calculations (section S3, and S4). In our main manuscript, we show the braiding process for positive sublattice potential $m > 0$ under the layer shifting as a braiding parameter. In section S4, we consider the negative sublattice potential $m < 0$ and discuss the braiding process. In section S5, we discuss the braiding process in AB stacking configuration and the notion of frame charge for this system. In section S6, we show the DFT band structure

of h-BX compound and the braiding process under pressure. In the section S7, we consider the effect of trigonal wrapping and discuss its importance on the braiding process. During the tuning of external braiding parameter the band nodes evolve in momentum space. As such the related edge modes also evolve in the boundary of the systems. In section S8, we shown the edge modes evolution when braiding parameters are continuously tuned. In section S9, we show the linking structure topology which comes as a results of braiding in parameters space.

S2. BRAIDING PROTOCOLS

The Dirac cones (DCs) in a two dimensional (2D) system with I_{ST} symmetry possess non-Abelian charges [1, 2]. In a suitable basis where $I_{ST} = \mathcal{K}$ (\mathcal{K} is a complex conjugation operator), the Hamiltonian of the system becomes real i.e., $H(k) = H^*(k)$ [3]. For such Hamiltonian with many energy bands (≥ 3), the underlying symmetry group has a non-Abelian group structure. For instance, a three-band Hamiltonian has the generic form of $H(k) = \sum_{n=1}^3 \epsilon_n |\psi_k^n\rangle \langle \psi_k^n|$, where $|\psi_k^n\rangle$ is a real orthonormal three component vector with $O(1)$ ambiguity. Therefore, the corresponding classifying space is $M_3 = O(3)/O(1)^3$ where $O(N)$ represents the orthonormal group. The homotopy group of the system is quaternion i.e., $\pi_1(M_3) = \mathbb{Q}$, a non-Abelian group which has five conjugacy classes $\{+1, -1, \pm i, \pm j, \pm ij\}$ with the anti-commuting relations $ij = -ji$ and $i^2 = j^2 = -1$ [2]. Therefore, the I_{ST} symmetric band nodes are characterized by the non-Abelian topological invariant, which serves the key ingredient for the non-Abelian braiding protocol and related charge conversion phenomena. In Fig. S1, we briefly illustrate how non-Abelian charges are introduced in the presence of DCs in a I_{ST} symmetric system.

In Fig. S1 (a-d) The square, star, and disk represent the Dirac cones (DCs) between different bands. For instance, if green nodes (disk and star) are DCs between bands 1 and 2 then the back node (square) represents the DCs between bands 2 and 3. Two loops c_1 and c_2 are considered to enclose a DC with a common base point at x_0 that allows the possibility of two different loops to combine together as shown in Fig. S1(a). c_1 and c_2 can not be smoothly converted to each

* bjyang@snu.ac.kr

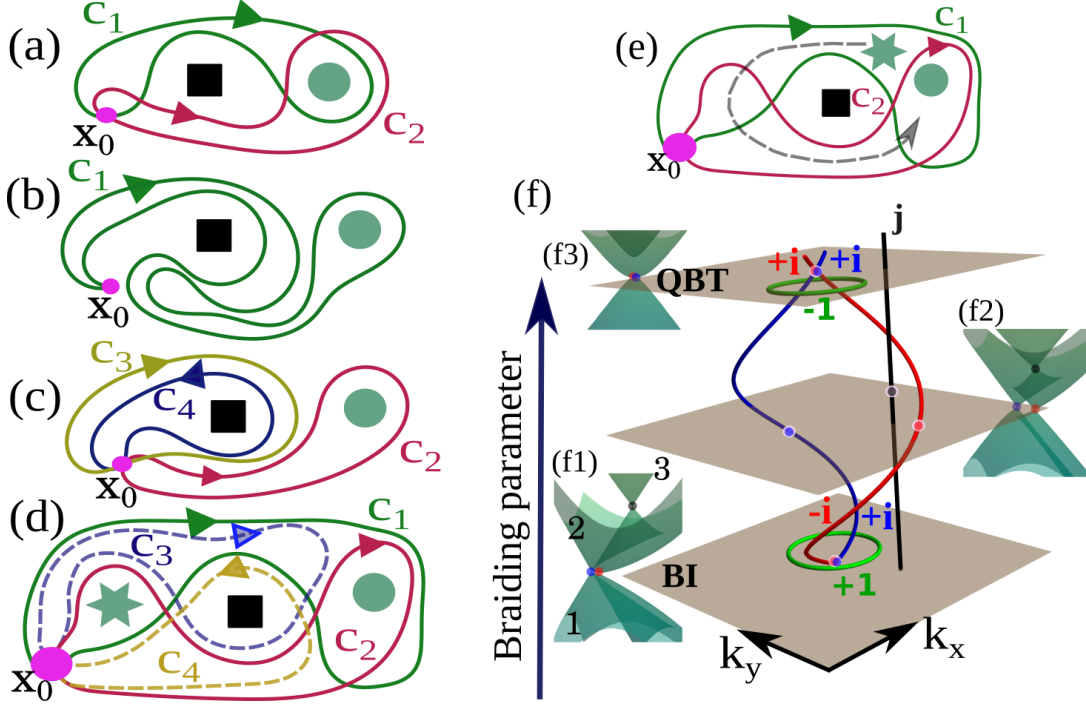


FIG. S1. (a-e) Non-Abelian braiding protocol in the presence of multiple Dirac nodes. (f1) The charge conversion of a pair of Dirac nodes of charges $+i$ and $-i$ between bands 1 and 2 which are created through a band inversion (BI). (f2) One of the nodes encircle a Dirac node of charge j between band 2 and 3 and convert the charge from $[+i, -i]$ to $[+i, -i]$ by braiding process.

other in of the presence of the black node. In Fig. S1(a-c), we show a smooth deformation of c_1 loop into three new loops as $c_1 \sim c_3 \circ c_2 \circ c_4 \sim c_3 \circ c_2 \circ c_3^{-1}$ ($c_4 \sim c_3^{-1}$). The “ \circ ” symbol represents the composition of two loops. For instance, $c_3 \circ c_2 \circ c_4$ in Fig. S1 (c) indicates that a composition has to be made by a journey starting at x_0 and traveling along c_3 than come back to x_0 then travel on c_2 and finally on c_4 . The “ \sim ” symbol represent that the combination loop on the two sides of the equation can be converted to each other smoothly. The possibility to compose the loops gives a group structure to the homotopy group whose elements represents as topological charges when calculated over a loop [4]. Now we denote the charge by the element of the first homotopy group over a loop c_i as $\pi_1^{c_i}$, we have $\pi_1^{c_1} = \pi_1^{c_3} \pi_1^{c_2} \pi_1^{c_3^{-1}}$. Let’s assume that $\pi_1^{c_2} = +i$ and $\pi_1^{c_3} = +j$ that gives $\pi_1^{c_1} = -i$. (d) Various loops to enclose three DCs. In this case, the loops have the relation as $c_1 \sim c_3 \circ c_2 \circ c_4$ which gives, $\pi_1^{c_1} = \pi_1^{c_3} \pi_1^{c_2} \pi_1^{c_4}$. Let’s now assume that the charge of two DCs inside the c_2 loop in (d) is same (say $(+i, +i)$ i.e., total charge -1) and charge of black DC on loop c_3 is $+j$, also we can write $c_3 \sim c_4$ from the analysis of (a-c). It immediately implies that the two DC have opposite charges $((+i, -i)$ i.e., total charge $+1$) if calculated on c_1 in contrast to the same charge i.e., $(+i, +i)$ on c_2 . As a result, two DCs can only be annihilated by taking them together inside c_1 loop but not inside the c_2 loop. The ability of such path dependent charge properties enables the braiding phenomena.

A schematic representation of a DC (green star) which is encircling another DC (black square) during the braiding pro-

cess S1(e). Figure. S1(f) shows a schematic braiding and charge conversion protocol in three band model where two Dirac nodes with opposite charges $(i, -i)$ are created by the band inversion (BI) between bands 1 and 2. Another DC exist between band 2 and 3 with charge j . One DC with charge $-i$ (indicated by red) encircle the DC with charge j (indicated by black) during the braiding parameter evolution and converts its charge from $-i$ to $+i$ and eventually meet with the blue DC with charge $+i$ and form a quadratic band touching (QBT) with total charge -1 . The green loop represents the charge-calculating loop enclosing two DCs. $+1$ (-1) represents the trivial (non-trivial) charge on the loops.

S3. DFT COMPUTATIONAL DETAILS

First principle calculations were carried out using projector augmented wave (PAW)[5] formalism based on Density Functional Theory (DFT) as implemented in the Vienna ab-initio Simulation Package (VASP).[6, 7] The generalized-gradient approximation by Perdew-Burke- Ernzerhof (PBE)[7] was employed to describe the exchange and correlation. An energy cut-off of 500 eV is used to truncate the plane-wave basis sets. The Brillouin zone (BZ) is integrated using $15 \times 15 \times 1$ Γ -centered k -mesh. DFT-D2 method has been applied for Van der Waals forces correction. Tight-binding (TB) Hamiltonians were constructed using maximally localized Wannier functions (MLWFs)[8–10] obtained from Wannier90 package[11].

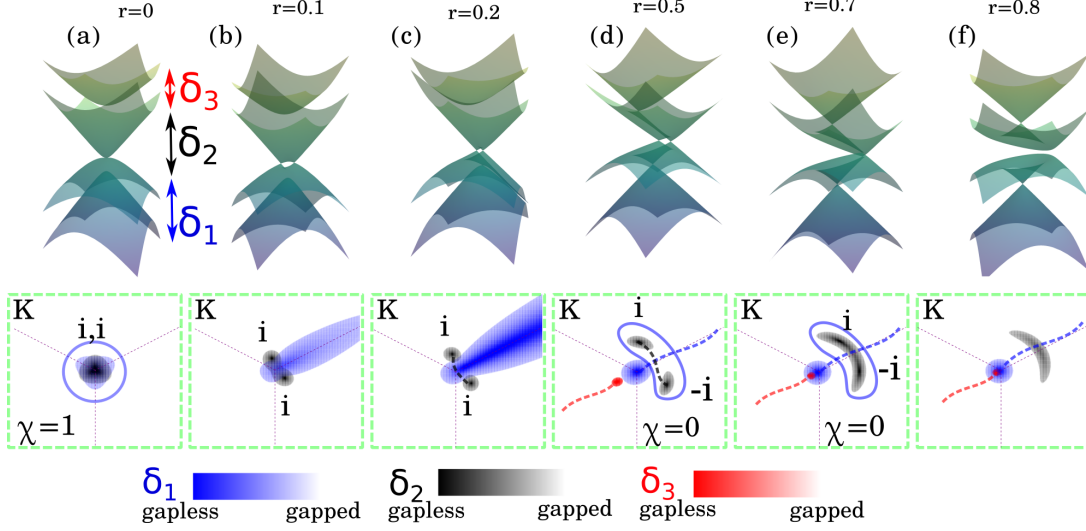


FIG. S2. (a-f) Energy dispersion around K (top panel) and nodal structures (bottom panel) for various shifting r and three gaps represented by δ_1 , δ_2 , and δ_3 between the bands. The sub-lattice potential $m = -0.1$ is used ($m = +0.1$ is used in Fig.2 of the main manuscript). In the bottom panel the closed loops represent the charge calculating loops for which patch Euler class χ is computed. The dashed lines represent Dirac strings, which can flip the topological charge of the adjacent Dirac node after crossing. Color bar at the bottom represents the gap size for three gaps δ_1 , δ_2 , and δ_3 .

S4. TIGHT-BINDING DETAILS

The Hamiltonian for p_z orbitals is written as,

$$H = \sum_{\langle i,j \rangle} t(\mathbf{r}_i - \mathbf{r}_j) |r_i\rangle \langle r_j| + h.c \quad (S1)$$

\mathbf{r}_i represents the position of i^{th} lattice site and $t(\mathbf{r}_i - \mathbf{r}_j)$ is the hopping between i^{th} and j^{th} sites which is given by [12, 13]

$$-t(\mathbf{r}) = V_\pi \left[1 - \left(\frac{\mathbf{r} \cdot \mathbf{e}_z}{R} \right)^2 \right] + V_\sigma \left(\frac{\mathbf{r} \cdot \mathbf{e}_z}{R} \right)^2. \quad (S2)$$

Here, $\mathbf{R} = \mathbf{r}_i - \mathbf{r}_j$, $V_\pi = V_\pi^0 e^{-\left(\frac{r-a_0}{\delta_0}\right)}$, $V_\sigma = V_\sigma^0 e^{-\left(\frac{r-h_0}{\delta_0}\right)}$. We use the band length $a_0 = 1.42\text{\AA}$, graphene's bond length, V_π^0 and V_σ^0 represent the transfer integral between the sites of intralayer and interlayer atoms whose values have been chosen as -2.7 eV and 0.48 eV. $\delta_0 = 0.318a_0$ is the decay length. We add a sub-lattice imbalance m in the two sites of each layer such a way it respect the structural inversion symmetry. Such sub-lattice imbalance mimic our model similar to the h-BX bi-layers (B=Boron, X=N (Nitrogen), P (Phosphorus), and As (Arsenic)).

In the main manuscript Fig. S2, we consider $m = +0.1$ and show that the two Dirac nodes in δ_2 gap braid with the Dirac node in δ_3 . Here, we consider $m = -0.1$ (Fig. S2) and show that the two braiding happens by the Dirac node of the δ_1 gap. Fig. S2 (a) shows that the presence of a quadratic band touching (QBT) in the δ_2 gap. The patch Euler class $\chi = 1$ of the QBT. The QBT can be consider as two Dirac nodes with charge $+i$ and $+i$. When r is increased, the QBT breaks in

two Dirac node and evolve in momentum space. During the process, the Dirac two nodes converts their charges to $+i$ and i (so the $\chi = 0$) through the braiding process by the blue node (bottom panel of Fig. S2 (d)). Further evolution annihilated the nodes (bottom panel of Fig. S2 (e-f)).

S5. FRAME CHARGE AND BRAIDING FOR AB STACKING

In Fig. S3(a,f), we show how two Dirac nodes with charge $(+i$ and $+i)$ convert their relative charges through non-Abelian braiding for a small shift i.e. $r \neq 0$. This has been discussed in main text Fig.4. In the main paper, we compute path Euler class χ to show the braiding process. In the following, we discuss about the braiding process for $r = 0$, i.e, when the system is in AB stacking. In this case, the frame charge calculation becomes unavoidable.

We also show that the AB stacking with $r = 0$ [Fig. S3(g)] shows a different type of non-Abelian braiding under pressure [Fig. S3(h-j)]. In this case, the system possesses the three-fold rotation symmetry C_{3z} which protects the QBT at the K/K' , making the visualization of the corresponding Dirac string and the charge conversion process difficult since two DNs are merged at the QBT. Under pressure, QBT in the δ_1 gap transfers to the δ_2 gap through a triple point degeneracy (TPD), as illustrated in Fig. S3(i). However, TPD makes it challenging to compute χ , which is strictly defined for systems with only two bands, necessitating the frame rotation charge calculation [1]. When two bands on a given patch are completely separated from the other bands, the χ and the frame charge have the same consequences. Under I_{ST} , the real eigenvectors form an orthonormal frame $f(k) =: \{|\psi_k^n\rangle\}$,

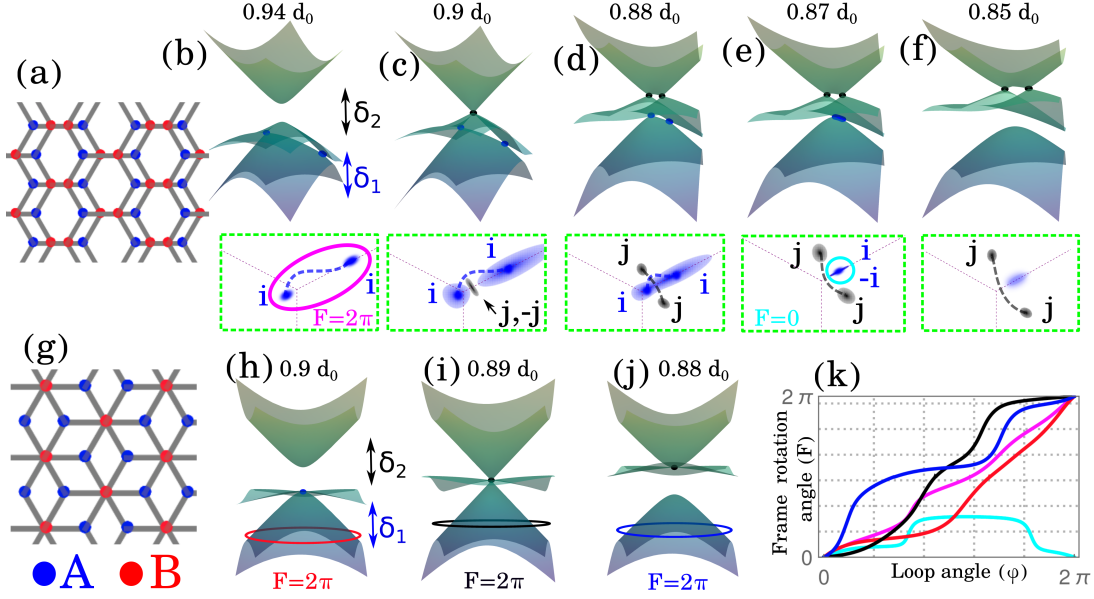


FIG. S3. Pressure-induced braiding. (a) A bilayer honeycomb lattice with a small shift ($r = 0.1$) of one layer from AB configuration. (b-f) The dispersion energy (upper panel) and configuration of the gapless region in momentum space near K point (lower panels) are plotted with decreasing interlayer distance (increasing pressure). d_0 is the interlayer distance of BLG. (g) AB configuration ($r = 0$) of a bilayer honeycomb lattice. (h-j) Dispersion energy of AB configuration with decreasing interlayer distance. (k) Frame rotation charge for the trajectory in various paths shown in (b) pink (e) cyan (h) red (i) black and (j) blue. In (b-f) and (h-j) we only show three lower bands of the energy dispersion and nodal configurations. The $\pm i$ and $\pm j$ represent charges of given DN in δ_1 and δ_2 , respectively.

well defined up to the \pm sign of each wave-function. For the orientable states $f(k) \in SO(N)$ where $\pi_1[SO(N)] = \mathbb{Z}_2$ for $N > 2$ [1, 2]. This \mathbb{Z}_2 frame charge can be defined as the accumulation of the total rotation angles over a loop enclosing the band nodes. If the accumulated rotation angle is 2π , the frame charge is non-trivial and the loop contains at least a pair of nodes with the same charge which can not be annihilated upon collision inside the loop. However, if the frame charge is trivial (accumulated rotation angle is 0), there are no nodes or pairs of nodes with the opposite charge that can be annihilated upon collision inside the loop [1]. We use the relation: $f(k)^T \cdot f(k_0) = \text{Exp}[\sum_{j=1}^6 \alpha_j L_j]$ to calculate the frame rotation angle for the BBHL four-band model. Here, α_j and L_j represent the Euler angles (the angle of rotations) and $SO(4)$ generators and the total frame rotation angle is defined as $F = \sqrt{\sum \alpha_j^2}$. The frame charge computed for different loops and the nodes are shown in Fig. S3(k). Here color of each line represent the charge on the loops, indicated by the same color in Fig. S3(b,e,h,i,j). Note that the frame charge for the given two nodes in Fig. S3(b) [pink loop] and Fig. S3(e) [cyan loop] are converted from 2π to 0 after braiding which is consistent the prediction based on Dirac strings. The TDP in Fig. S3(i) has 2π frame charge as expected since the two DN's have the same charges. Therefore transporting QBT from the lower to the middle gap through the TPD can be considered an instantaneous braiding process.

S6. DFT SIMULATIONS FOR H-BX (B=BORON, X= P (PHOSPHORUS), AND AS (ARSENIC))

We perform *first principle calculations* based on Density Functional Theory (DFT) within generalized-gradient approximation using the Vienna Ab-initio Simulation Package (VASP). Motivated by the tight-binding model from the previous section, we choose two-dimensional system h-BX (B=Boron, X=N (Nitrogen), P (Phosphorus), and As (Arsenic)) for the DFT calculations. The AB and AA stacking is shown in Fig. S4 (a). The binary element of these system indicates different onsite potentials due to different atomic characteristics and induces imbalance to sublattice potential m . The electronic structure of h-BN, h-BP, and h-BAs are topologically similar, only differ by the size of the band gap as the strength of sub-lattice potentials m are different for them. For instance, the value of m is maximum for h-BN and it is lowest for h-BAs. As a result the band gap of h-BN is highest (around 4.5 eV) and it is lowest for h-BAs (around 0.5 eV). Here, we choose h-BP as one of the representative of the above mentioned system and compute the band structure. We apply vertical pressure which works as a braiding parameter for this system. Fig. S4 (b-f) shows the band structure (near K valley) evolution (top panel) and its nodal positions (bottom panel) under increasing pressure. Here we only show the three band for which the Dirac nodes are represented by the black and blue disks. To apply the pressure, we decrease the interlayer distance and computed the resultant pressure in the system from Ab-initio calculations. Fig. S4(b) shows the presence of two Dirac nodes between the two lower bands whose

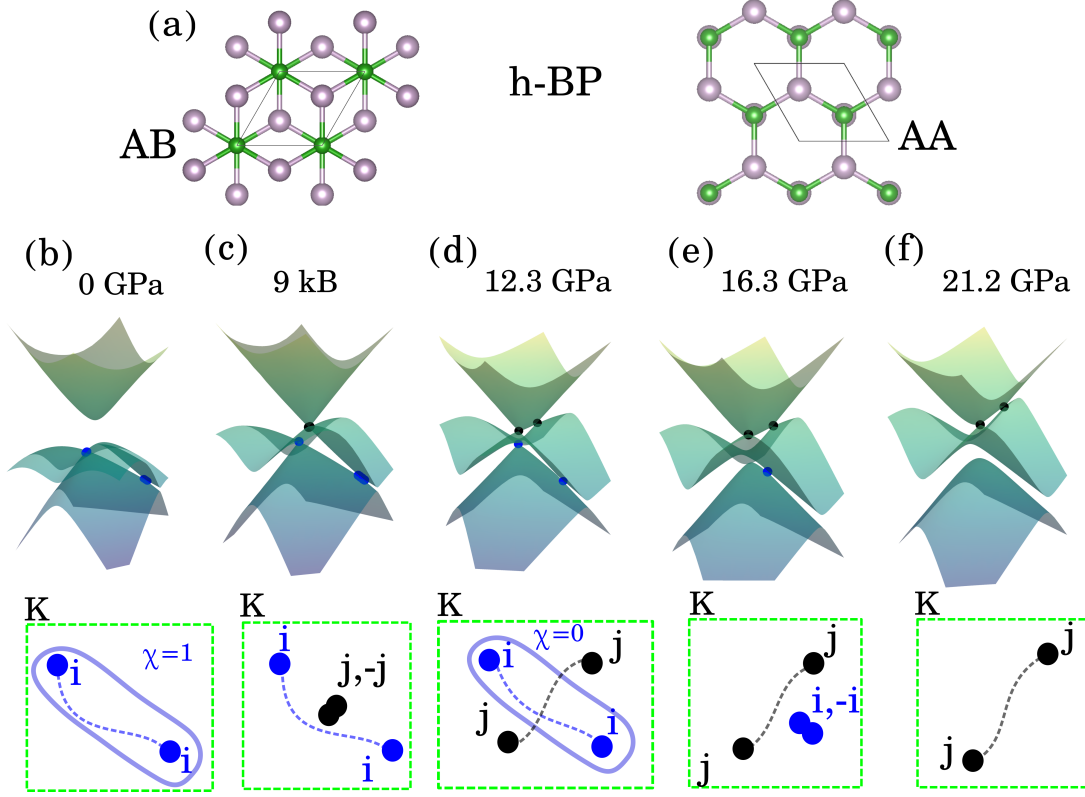


FIG. S4. (a) Bi-layer h-BP AB stacking (top panel) and AA stacking (bottom panel). (b-f) Band (top panel) and nodal (bottom panel) structure evolution under the external vertical pressure for a stacking which is slightly shifted from AB stacking towards AA stacking. The black and blue disks represent the nodes between upper two and lower two bands. The dashed line represent the Dirac string between the nodes. Patch Euler class χ is computed over the loop represented by blue color.

path Euler class $\chi = 1$ over a loop. This means that the two nodes are topologically robust i.e., they can not be annihilated by taking them together inside the loop. However, when pressure is increased, two more nodes with opposite charge are created (the black nodes) through a band inversion between the upper two bands. Eventually, one of the black nodes crosses the Dirac string of blue nodes and converts their mutual charges as depicted in the bottom panel of Fig. S4 (b-f). Note that the charge of the two blue nodes is initially (Fig. S4 (a)) the same i.e., $+i$ and $+i$ (so the $\chi = 1$) which becomes opposite i.e., $+i$ and $-i$ (so the $\chi = 0$) (Fig. S4 (d)). This non-trivial charge conversion by the Non-Abelian braiding allows two blue nodes (whose charge was initially same) to annihilate at the end (Fig. S4 (e)). In the meantime, the two black nodes whose charge was opposite (Fig. S4 (c)), become the same (Fig. S4 (f)) eventually. In this process, two nodes from one gap transport to another gap by Non-Abelian braiding.

S7. EFFECT OF TRIGONAL WRAPPING

In our all calculations, we show that the QBT appears when $r = 0$. However, this QBT is not in general stable. This is because of the presence of the C_3 symmetric wrapping term which comes from the higher order hopping in the system. Al-

though such higher order hopping strength is in general very small, we can not neglect such effect. If we zoom out momentum space near the K point for $r = 0$, we find that the band structure actually possesses four Dirac nodes instead of a QBT. However, such nodal configurations do not change our discussion regarding the non-Abelian braiding.

For $r = 0$, the system is AB stacking and possesses the C_3 rotation symmetry which is manifested in the nodal structure also (in bottom panel of Fig S5 (b)). In this case, there are four nodes (one at the K point and other three sitting in a C_3 symmetric way) of charge $+i$, $+i$, $+i$, and $-i$. Note that, if we combine these four nodes together, they effectively give a total charge of -1 which is the combination of two Dirac nodes with the same charge. Therefore, considering two Dirac nodes of charge $+i$, $+i$ and four nodes of charges $+i$, $+i$, $+i$, and $-i$ topologically equivalent. In fact, in Fig. S5(b-f) shows that the four nodes which have $+i$, $+i$, $+i$, and $-i$ charge converted to two nodes of charge $+i$, $+i$ for a very small layer shifting. As such, considering the QBT or the four Dirac nodes at the beginning of the nodal evolution for non-Abelian braiding process conclude the same results.

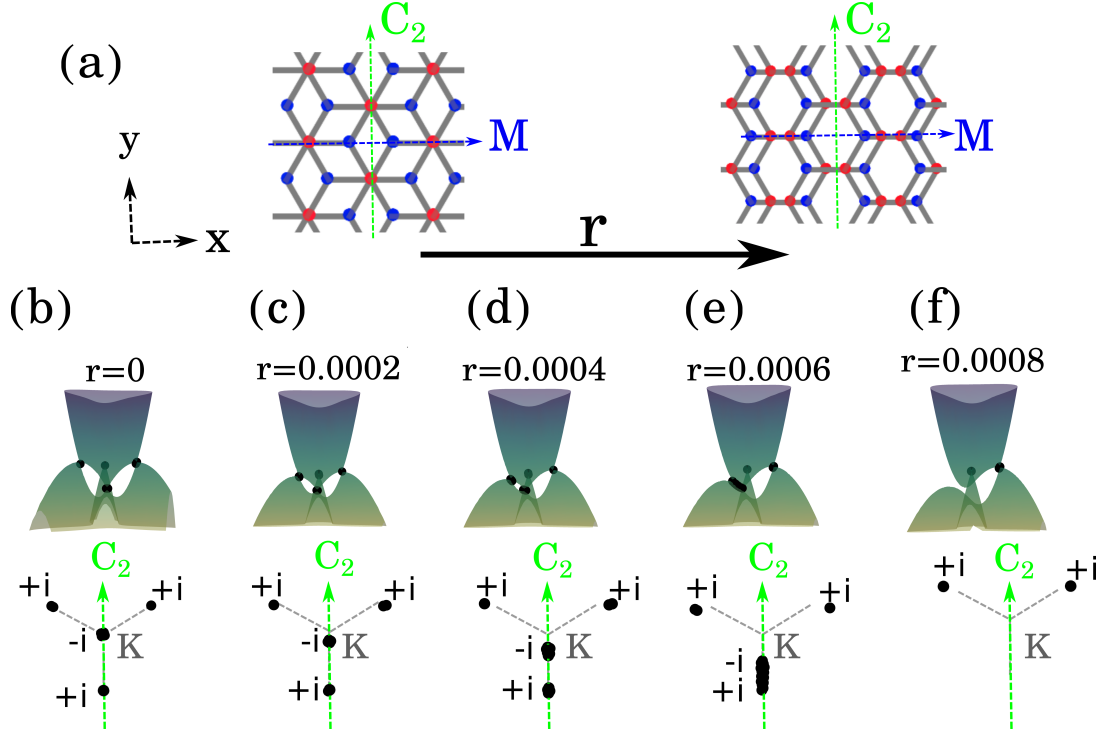


FIG. S5. Effect of trigonal wrapping. (a) BLGT lattice when layer shifting is zero (left) and one layer is slightly shifted from other (right). When layer shifting is zero, the system have C_3 rotation symmetry about the the z -axis and C_3 is broken when one layer is shifted. For both cases, two fold rotation C_2 about y -axis and a mirror along x is present. (b-f) shows the band structure very near to the K point for different r . For $r = 0$, the system is AB stacking and possess the C_3 rotation symmetry which is manifested in the nodal structure also (in bottom panel of (b)). In this case, there are four nodes (one at the K point and other three sitting in a C_3 symmetric way). When there is a slight shifting and r is increased, two of the nodes with opposite charge come together in a C_2 symmetric way and annihilate. Other two nodes with same charge remain.

S8. EDGE MODE EVOLUTION DURING BRAIDING PARAMETERS TUNING

The Dirac cone carries a nontrivial π -Berry phase, which leads to the emergence of edge mode. An well-known example of this phenomenon occurs in the zigzag edges of graphene. In our study, we start with a QBT at the AB stacking configuration. Such QBT does not possess non-trivial Berry phase. As such it does not provide protected edge modes in the boundary of the system. However, during the braiding the QBT breaks into two Dirac cones in both the K and K' valleys [see Fig. S6]. The separation of the Dirac nodes at each valley generates edge modes between them. This is because of the non-trivial π -Berry phase that developed between the two Dirac nodes which comes from QBT in each valleys. As we have discussed in the main manuscript (Fig. 2) and in Fig. S2 that the QBT breaks into two Dirac nodes and the first increase the distance between them approximately up to $r = 0.5$ and then come closer and marge together to annihilate. The correspondence of the movement of bulk Dirac cone at the edge as follows; first an edge mode emerges between two Dirac node which comes from QBT and the edge modes start becoming larger in momentum space approximately up to $r = 0.5$. After that the edge modes sinks as the separation of the Dirac nodes decrease. Finally, two Dirac nodes

in bulk collide and annihilate which also removes the edge modes completely from the boundary.

In Fig. S6, we computed the egde modes for three different type of edge terminations; (i) armchair 30° (Fig. S6(a)), (ii) 46.96° (Fig. S6(b)), and (iii) zigzag 60° (Fig. S6(c)). The red and blue line represents the periodic and non-periodic direction of the systems. (a2-a7) Shows the evolution of edge modes from QBT at AB stacking (a7) to AA stacking (a2). In this case, the two valleys K and K' are projected in the same momentum point along the 1D Brillouin zone (BZ) of ribbon. However as r increases, we observe the edge modes from both valleys. The edge modes first become larger and then eventually shrink and vanish, once the two Dirac cone annihilate in bulk. Fig. S6(b2-b7) shows the edge modes for 46.96° edges where two valleys K and K' are separately projected on the 1D ribbon BZ. The evolution of the edge modes are also similar like the armchair edges. We also show the edge modes evolution for zigzag edges (c2-c7) which shows similar behavior like the other edges. In the zigzag case, we only show the edge bands corresponding to one valley of the bulk. The edge modes from other valley shows exactly same behavior.

The existence of such edge modes can diagnose the stage of braiding, as the separation of two Dirac cones results in an increased local density of states at the edges. This serves as a

clear indication of the braiding process, with the distinct Dirac cones contributing to enhanced edge localization.

S9. NODAL TRAJECTORIES FOR DIFFERENT SUBLATTICE POTENTIALS AND LAYER DISTANCE

In Fig. S7, the nodal trajectories are shown for varying sublattice potentials m and layer distance ratios $\alpha = h_z/h_z^0$, where h_z represents the layer distance and h_z^0 is the original distance in bilayer graphene. Decreasing α act as a increasing pressure. The colored lines depict the evolution of DN in the gaps δ_1 [blue], δ_2 [black], and δ_3 [red], as a function of

the shift parameter r (vertical direction) in momentum space (horizontal plane) near the K/K' points. The values $r = 0$ and $r = 1$ correspond to AB and AA stacking configurations, respectively. At $m = 0$, a nodal line configuration appears at AA stacking ($r = 1$) [the black loop at the top of $m = 0$ panels in Fig. S7], and a QBT occurs at AB stacking ($r = 0$), where both red and blue DN pass through. Introducing a small sublattice potential m eliminates the nodal line, resulting in a loop that contains either the red or blue DN trajectory. As $|m|$ increases, the QBT at AB stacking is eliminated from the black DN, and it transfers to the red or blue DN using a braiding process. However, applying pressure (decreasing α) can bring it back again.

-
- [1] A. Bouhon, Q. Wu, R.-J. Slager, H. Weng, O. V. Yazyev, and T. Bzdušek, Non-abelian reciprocal braiding of weyl points and its manifestation in zrte, *Nature Physics* **16**, 1137 (2020).
 - [2] Q. Wu, A. A. Soluyanov, and T. Bzdušek, Non-abelian band topology in noninteracting metals, *Science* **365**, 1273 (2019), <https://www.science.org/doi/pdf/10.1126/science.aau8740>.
 - [3] J. Ahn, S. Park, and B.-J. Yang, Failure of nielsen-ninomiya theorem and fragile topology in two-dimensional systems with space-time inversion symmetry: Application to twisted bilayer graphene at magic angle, *Phys. Rev. X* **9**, 021013 (2019).
 - [4] N. D. Mermin, The topological theory of defects in ordered media, *Rev. Mod. Phys.* **51**, 591 (1979).
 - [5] P. E. Blöchl, Projector augmented-wave method, *Phys. Rev. B* **50**, 17953 (1994).
 - [6] G. Kresse and J. Hafner, Ab initio molecular dynamics for liquid metals, *Phys. Rev. B* **47**, 558 (1993).
 - [7] G. Kresse and D. Joubert, From ultrasoft pseudopotentials to the projector augmented-wave method, *Phys. Rev. B* **59**, 1758 (1999).
 - [8] N. Marzari and D. Vanderbilt, Maximally localized generalized wannier functions for composite energy bands, *Phys. Rev. B* **56**, 12847 (1997).
 - [9] I. Souza, N. Marzari, and D. Vanderbilt, Maximally localized wannier functions for entangled energy bands, *Phys. Rev. B* **65**, 035109 (2001).
 - [10] N. Marzari, A. A. Mostofi, J. R. Yates, I. Souza, and D. Vanderbilt, Maximally localized wannier functions: Theory and applications, *Rev. Mod. Phys.* **84**, 1419 (2012).
 - [11] A. A. Mostofi, J. R. Yates, G. Pizzi, Y.-S. Lee, I. Souza, D. Vanderbilt, and N. Marzari, An updated version of wannier90: A tool for obtaining maximally-localised wannier functions, *Computer Physics Communications* **185**, 2309 (2014).
 - [12] G. Trambly de Laissardière, D. Mayou, and L. Magaud, Localization of dirac electrons in rotated graphene bilayers, *Nano Letters* **10**, 804 (2010).
 - [13] P. Moon and M. Koshino, Optical absorption in twisted bilayer graphene, *Phys. Rev. B* **87**, 205404 (2013).

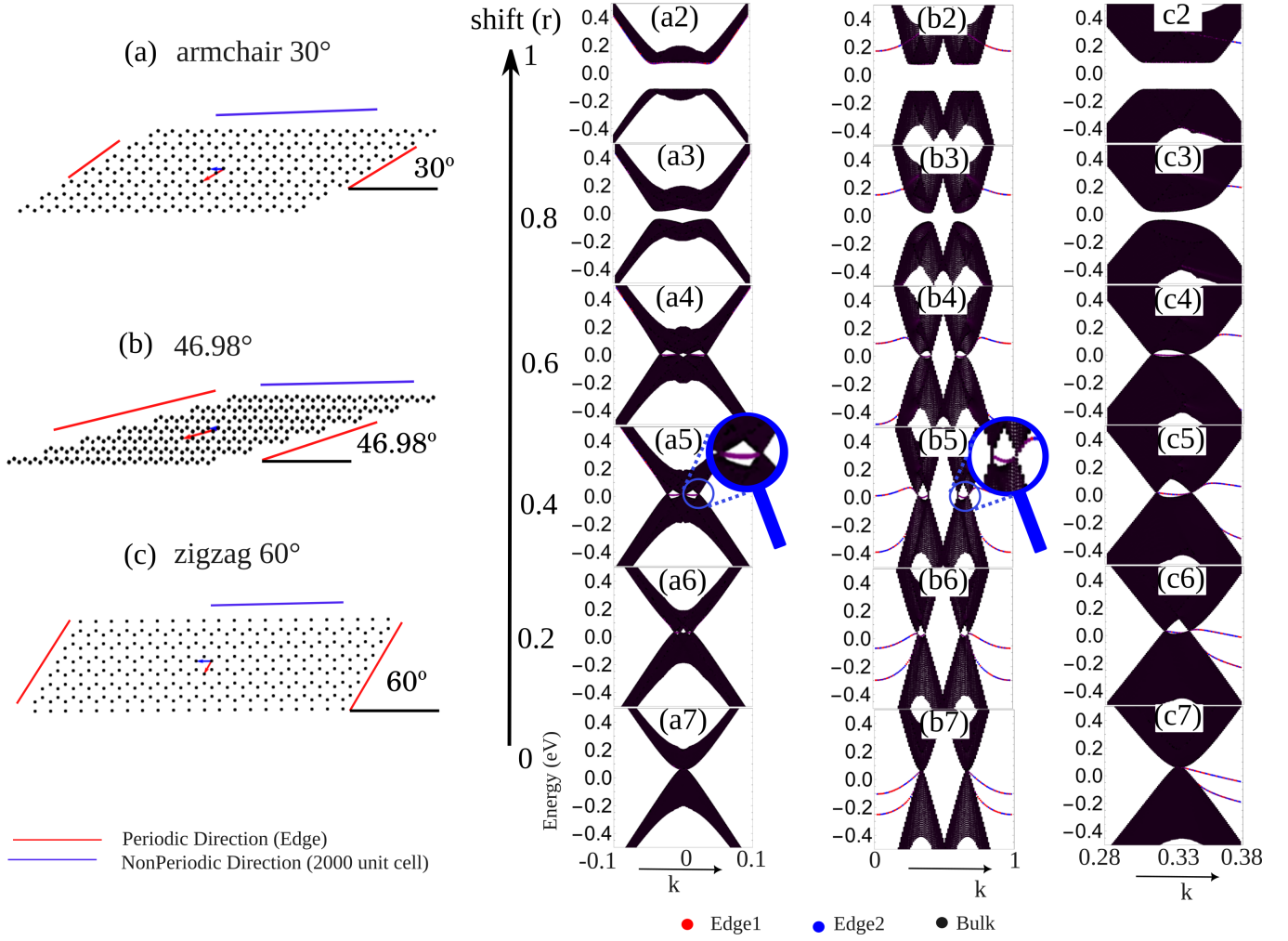


FIG. S6. Slab energy dispersion for (a) 30° (armchair), (b) 46.98°, and (c) 60° (zigzag) direction edges. Red (blue) lines indicate periodic (non-periodic) directions. Arrows inside (a), (b), and (c) represent the unit cell. The colors in (a2-a7), (b2-b7), and (c2-c7) indicate the wavefunction characteristics, where red, blue, and black correspond to top edge, bottom edge, and bulk modes respectively. Magnifiers display zoomed-in plots. In (a2-a7), (b2-b7), and (c2-c7), the horizontal axis represents momenta in units of the slab's 1D Brillouin zone. The strength of sublattice potential is given as $m = 0.1$.

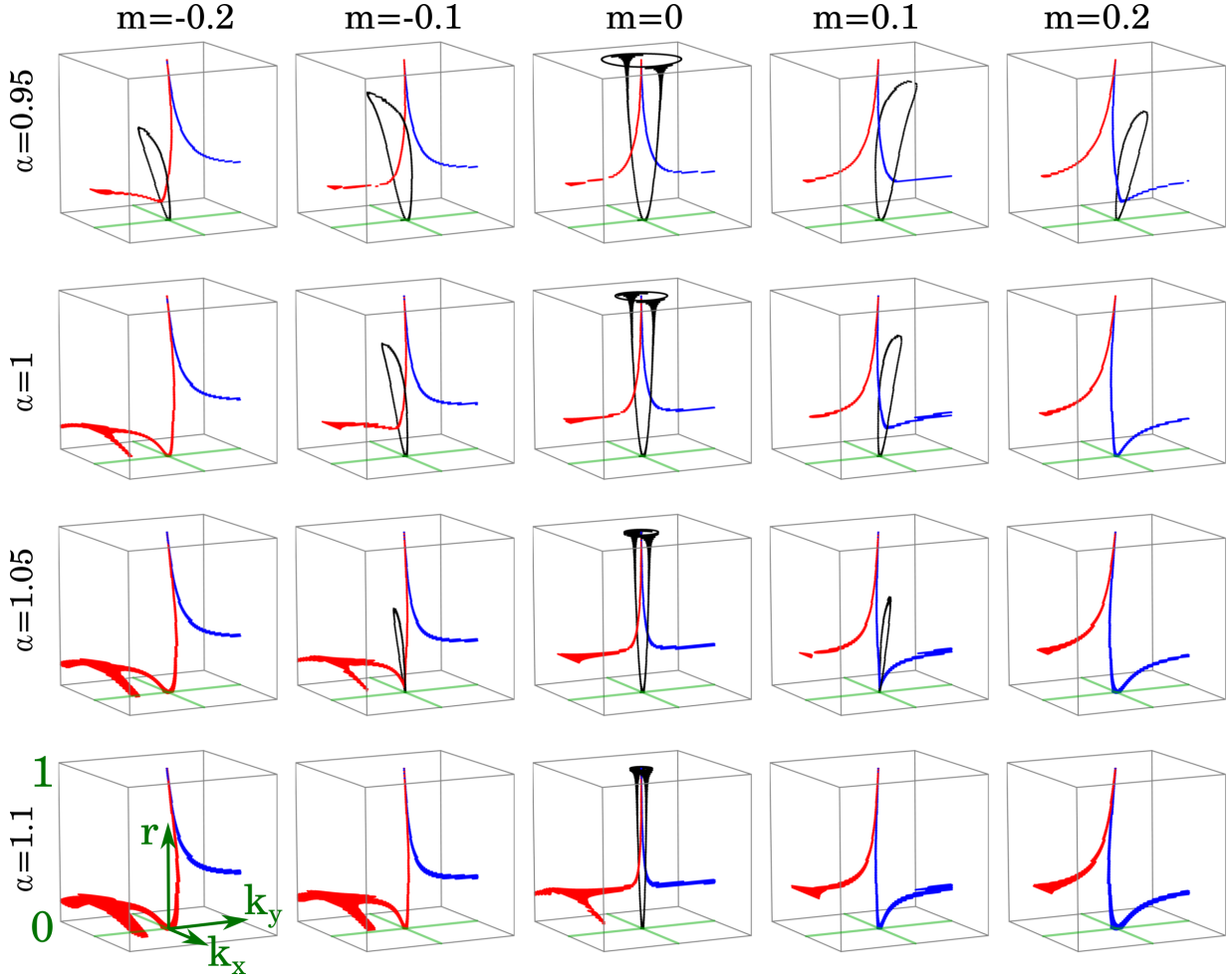


FIG. S7. Nodal trajectories for different sublattice potentials m and layer distance ratios $\alpha = h_z/h_z^0$, where h_z is the layer distance and h_z^0 is the original distance in graphene. The colored lines represent the evolution of DNs in the gaps δ_1 [blue], δ_2 [black], and δ_3 [red], as a function of layer shifting (vertical direction, r) in momentum space (horizontal plane) near the K/K' points. The values $r = 0$ and $r = 1$ correspond to AB and AA stacking configurations, respectively. At $m = 0$, the system exhibits a nodal line configuration at AA stacking ($r = 1$) and a quadratic band touching (QBT) at AB stacking ($r = 0$), where both red and blue DNs pass through. With a small sublattice potential m , the nodal loop is eliminated, and the trajectory becomes a loop containing only one of the red or blue DN trajectories. As $|m|$ increases, the QBT at AB stacking is eliminated from the black DNs, and it transfers to the red or blue DN using a braiding process. However, applying pressure (decreasing α) can bring it back again.